

# High Temperature Electrolysis Using Electrode-Supported Cells

European Fuel Cell Forum 2010

J. E. O'Brien  
C. M. Stoots

July 2010

The INL is a  
U.S. Department of Energy  
National Laboratory  
operated by  
Battelle Energy Alliance



This is a preprint of a paper intended for publication in a journal or proceedings. Since changes may be made before publication, this preprint should not be cited or reproduced without permission of the author. This document was prepared as an account of work sponsored by an agency of the United States Government. Neither the United States Government nor any agency thereof, or any of their employees, makes any warranty, expressed or implied, or assumes any legal liability or responsibility for any third party's use, or the results of such use, of any information, apparatus, product or process disclosed in this report, or represents that its use by such third party would not infringe privately owned rights. The views expressed in this paper are not necessarily those of the United States Government or the sponsoring agency.

# High Temperature Electrolysis using Electrode-Supported Cells

**J. E. O'Brien, C. M. Stoots**  
Idaho National Laboratory  
2525 N. Fremont Ave., MS 3870  
Idaho Falls, ID USA  
Tel.: +001-208-526-9096  
james.obrien@inl.gov

## Abstract

An experimental study is under way to assess the performance of electrode-supported solid-oxide cells operating in the steam electrolysis mode for hydrogen production. The cells currently under study were developed primarily for the fuel cell mode of operation. Results presented in this paper were obtained from single cells, with an active area of 16 cm<sup>2</sup> per cell. The electrolysis cells are electrode-supported, with yttria-stabilized zirconia (YSZ) electrolytes (~10 µm thick), nickel-YSZ steam/hydrogen electrodes (~1400 µm thick), and manganite (LSM) air-side electrodes (~90 µm thick). The purpose of the present study was to document and compare the performance and degradation rates of these cells in the fuel cell mode and in the electrolysis mode under various operating conditions. Initial performance was documented through a series of DC potential sweeps and AC impedance spectroscopy measurements. Degradation was determined through long-duration testing, first in the fuel cell mode, then in the electrolysis mode over more than 500 hours of operation. Results indicate accelerated degradation rates in the electrolysis mode compared to the fuel cell mode, possibly due to electrode delamination. The paper also includes details of the single-cell test apparatus developed specifically for these experiments.

## Introduction

There is a growing interest in the development of large-scale non-fossil hydrogen production technologies. In terms of the transportation sector, this interest is driven by the near-term demand for hydrogen for refining of increasingly low-quality petroleum resources, the expected intermediate-term demand for carbon-neutral synthetic fuels, and the potential long-term demand for hydrogen as an environmentally benign direct transportation fuel (1) - (3). Additional important non-transportation markets for large-scale hydrogen production include ammonia production and (potentially) carbon-free steel production (4). At present, hydrogen production in North America is based almost exclusively on steam reforming of methane. From a long-term perspective, methane reforming may not be sustainable for large-scale hydrogen production since natural gas is a non-renewable resource that exhibits large volatility in price and since methane reforming and other fossil-fuel conversion processes emit large quantities of greenhouse gases to the environment (5). Non-fossil carbon-free options for hydrogen production include conventional water electrolysis coupled to either renewable (e.g., wind) energy sources or nuclear energy. The renewable-hydrogen option may be viable as a supplementary source, but would be very expensive as a large-scale stand-alone option (6), (7). Conventional electrolysis coupled to nuclear base-load power can approach economical viability when combined with off-peak power, but the capital cost is high (8). To achieve higher overall hydrogen production efficiencies, high-temperature

thermochemical [(9)] or electrolytic (10) processes can be used. The required high temperature process heat can be based on concentrated solar energy (11) or on nuclear energy from advanced high-temperature reactors (12). From 2003 – 2009, development and demonstration of advanced nuclear hydrogen technologies were supported by the US Department of Energy under the Nuclear Hydrogen Initiative (13). High temperature steam electrolysis was demonstrated as a feasible technology under this program, which included a 15 kW HTE technology demonstration, achieving a hydrogen production rate in excess of 5000 NL/hr (14). During 2009, the NHI program sponsored a technology down-selection activity by which an independent review team recommended HTE as the most appropriate advanced nuclear hydrogen production technology for near-term deployment (15). HTE research is currently supported by the DOE Office of Nuclear Energy under the Next Generation Nuclear Plant (NGNP) Program (12).

The ultimate cost of hydrogen production by any technology is dependent on both capital and operating costs. In order to achieve competitive capital costs, HTE cells and stacks must exhibit both high performance and low degradation rates. Although HTE has been successfully demonstrated, our experience to date has indicated that SOEC cell and stack degradation must be improved prior to deployment of HTE as a viable cost-competitive technology. Consequently, the current focus of our research is to identify the mechanisms responsible for accelerated degradation in the electrolysis mode. Once these mechanisms are fully understood and ranked in terms of importance, effective mitigation strategies can be developed. Possible degradation mechanisms include transport of impurities leading to electrode poisoning and deactivation (16), coarsening of electrodes (17), loss of electrolyte ionic conductivity (18), depletion of oxygen vacancies in mixed conducting electrodes (19), (20), and electrode delamination (21).

Anode-supported cells represent the state of the art for solid oxide fuel cells. In the electrolysis mode, the nickel cermet electrode becomes the cathode. Operation of these cells in the electrolysis mode can result in accelerated degradation and delamination of the oxygen electrode. The 5 cm x 5 cm electrode-supported single electrolysis cells tested to date have yttria-stabilized zirconia (YSZ) electrolytes (~10  $\mu\text{m}$  thick), nickel-YSZ steam/hydrogen electrodes (~1400  $\mu\text{m}$  thick), and manganite (LSM) air-side electrodes. The experiments were performed over a range of steam inlet mole fractions (0.03 – 0.6), gas flow rates, and current densities (0 to 0.6 A/cm<sup>2</sup>). Steam consumption rates associated with electrolysis were measured independently using inlet and outlet dewpoint instrumentation. On a molar basis, the steam consumption rate is equal to the hydrogen production rate. Initial cell performance was evaluated by performing DC potential sweeps at 900°C. The voltage-current characteristics are presented, along with values of area-specific resistance as a function of current density. Long-term cell performance is also assessed to evaluate cell degradation. Details of the apparatus we recently developed for testing of single electrode-supported cells will also be presented.

## 1. Experimental Apparatus

The test fixture and test stand designed for performance evaluation of electrode-supported single cells will now be described. This version of the test fixture is designed to evaluate the performance of individual cells without the complicating effects of interconnects. A modified version of this test fixture could be used to test individual cells plus interconnects.

Referring to the exploded view provided in Fig. 1, a steam hydrogen mixture enters through a 1/4-in inconel coiled tube into the inlet hole in the bottom of the Hastelloy-X (HastX) base plate. It then flows through a diverging flow channel milled into the HastX base plate and passes through a slot in the bottom of the alumina cell holder. The slots can be seen in Fig 2. An alumina felt gasket is used to seal the HastX base plate against the alumina cell holder. The flow then passes under the cell through a

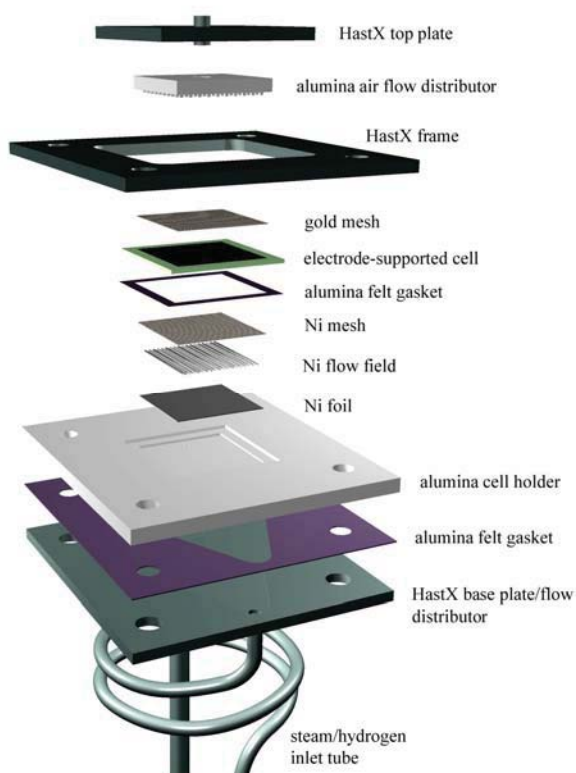


Figure 1. Exploded view of cell fixture.

bottom of the alumina cell holder, visible in Fig. 2(a).

After passing along the bottom of the cell, the steam/hydrogen flow exits the alumina cell holder through a second slot, flows through a converging passage in the HastX base plate, and out through an 3/8-in OD inconel outlet tube. The outlet tube is sized larger than the inlet tube in order to minimize back pressure on the cell seals.

The cell is placed on a shelf milled into the alumina cell holder just above and in contact with the Ni mesh (see Fig. 2 (b)). The cell dimensions are 5 cm x 5 cm, 1.5 mm thick. A nickel paste was used to enhance electrical contact between the cell and the nickel mesh, flow field, and foil. An alumina felt gasket is placed on the shelf underneath the cell to help with sealing. In addition, for sealing, an alumina-based ceramic paste (Aremco Products, Ceramabond 552) is distributed around the top outer edge of the cell to

corrugated/perforated nickel flow field. The flow field establishes the gap for the steam/hydrogen flow channel under the cell while also serving as an electrical conductor. A 0.254 mm (0.010 in) nickel foil underneath the flow field serves as a current collector. The Ni foil, flow field, and mesh are sized to fit into the inner square recess machined into the alumina cell holder. Alumina was selected as the cell holder and air flow distributor material in order to minimize the potential for chromium poisoning of the cell electrodes. The cell holder was machined in the bisque state and then fired. During firing the bisque alumina shrinks by about 15%. This shrinkage must be taken into account when doing the machining such that the desired dimensions are achieved in the final dense alumina part.

A gold wire in direct contact with the nickel foil serves as the steam/hydrogen-side power lead and voltage tap. The wire just fits in one of the grooves of the flow field. The two ends of this wire are fed out through the two small holes shown in the

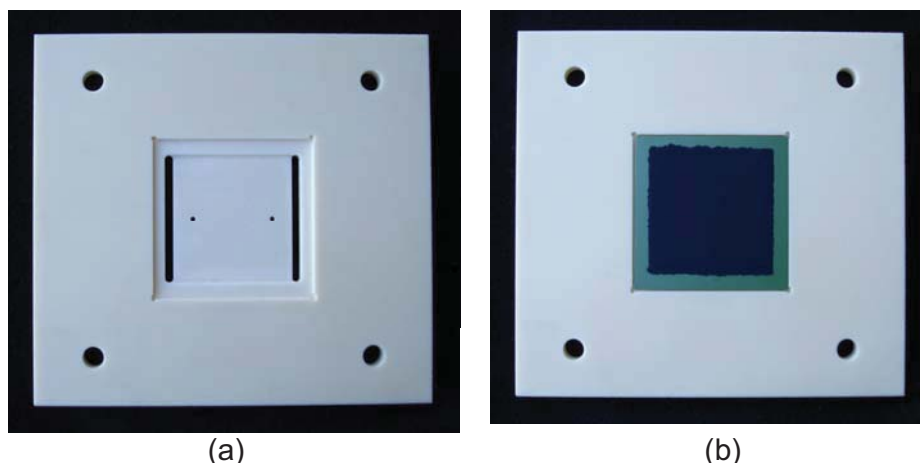


Figure 2. (a) alumina cell holder; (b) cell holder with cell in place.

seal the gap between the cell and the alumina cell holder.

On the air side of the cell, a gold mesh contacts the air-side electrode. This gold mesh is held against the air-side electrode by the alumina air flow distributor. The air flow distributor has an array of square protuberances milled into its surface (see Fig. 3), creating a gap for air flow while also compressing the gold mesh against the air-side electrode. A gold wire is positioned in one of the grooves, in contact with the gold mesh, for current collection. One end of this wire is used as a power lead and the other end is used as a voltage tap.

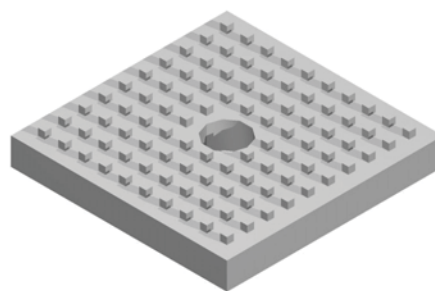


Figure 3. Alumina air flow distributor.

Air is introduced to the top side of the cell through an inlet tube welded to the HastX top plate. This tube protrudes slightly into a central hole in the alumina air flow distributor. A seal was formed between the HastX top plate and the alumina air flow distributor by means of an alumina felt gasket. After exiting the central hole in the air flow distributor, the air impinges on the cathode side of the cell and flows radially outward through the array of protuberances. The air then exits into the furnace volume.

A fixed compressive load is applied to the entire cell stackup between the alumina cell holder and the HastX top plate by means of weights, as shown in the test stand overview, Fig. 4. This load simultaneously compresses the cell against the nickel mesh, flow field and foil on the bottom steam/hydrogen side of the cell and against the gold mesh on the air side. It also compresses the cell against the seal around the outer edge of the cell which rests on the shelf milled into the alumina cell holder. The HastX weight plates are held in alignment by the upper portion of the threaded rods which extend upward for this purpose.

A fixed compressive load is independently applied between the HastX frame, the alumina cell holder, and the HastX base plate. This load is generated by the compression of four springs located under the test stand base support outside of the furnace. The springs will be compressed a fixed amount that is determined by the height of the spool pieces by tightening a nut on the threaded rods. The threaded rods are fed through the alumina spacer tubes. These spacer tubes determine the height of the cell holder inside the furnace. The spring-generated load is intended to compress the seal between the cell holder and the base plate. This seal was formed by alumina felt impregnated with alumina slurry. A nut is visible on the threaded rods in Fig. 4 just above the HastX frame and below the weight plates. This nut represents the upper stop for this compressive load. The extension of the threaded rods above the nuts is for the purpose of aligning the weight plates. Note that the weight plates are floating above these nuts since they are resting on the

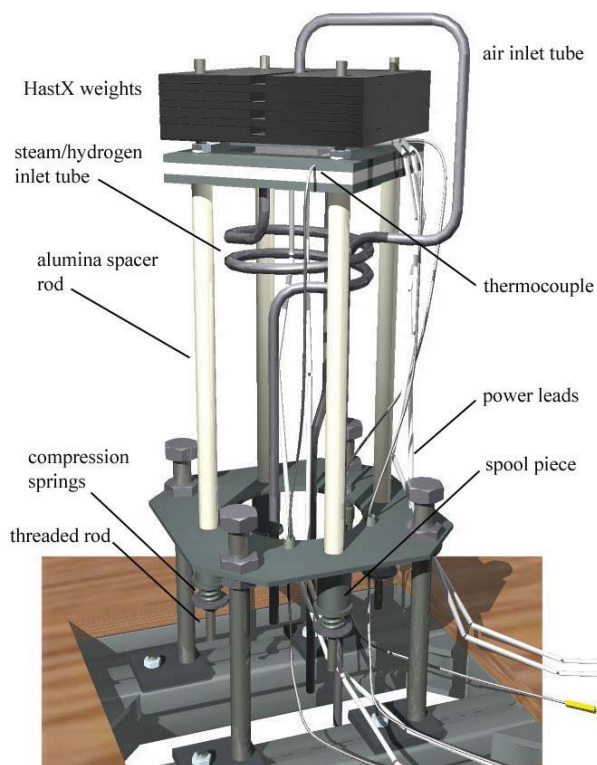


Figure 4. Test stand overview.



HastX top plate.

A photograph of the test stand installed in the furnace base is provided in Fig. 5. Note that the base support is located outside of the furnace. Holes were drilled in the bottom of the kiln for pass-through of the flow tubes, the alumina spacer rods, power leads and instrumentation.

A process flow diagram for the experimental apparatus used for single-cell testing is presented in Fig. 6. Primary components include gas supply cylinders, mass-flow controllers, a heated water-bath humidifier, on-line dewpoint sensors, temperature and pressure measurement, high temperature furnace, and the solid oxide electrolysis cell. Nitrogen is used as an inert carrier gas. Inlet flow rates of nitrogen, hydrogen, and air are established by means of precision mass-flow controllers. Hydrogen is included in the inlet flow as a reducing gas in order to prevent oxidation of the Nickel cermet electrode material. Air flow to the cell is supplied by the shop air system, after passing through a two-stage extractor / dryer unit. The cathode-side inlet gas mixture, consisting of hydrogen and nitrogen is mixed with steam by means of a heated humidifier. The dewpoint temperature of the nitrogen / hydrogen / steam gas mixture exiting the humidifier is monitored continuously using a precision dewpoint sensor. All gas lines located downstream of the humidifier are heat-traced in order to prevent steam condensation.

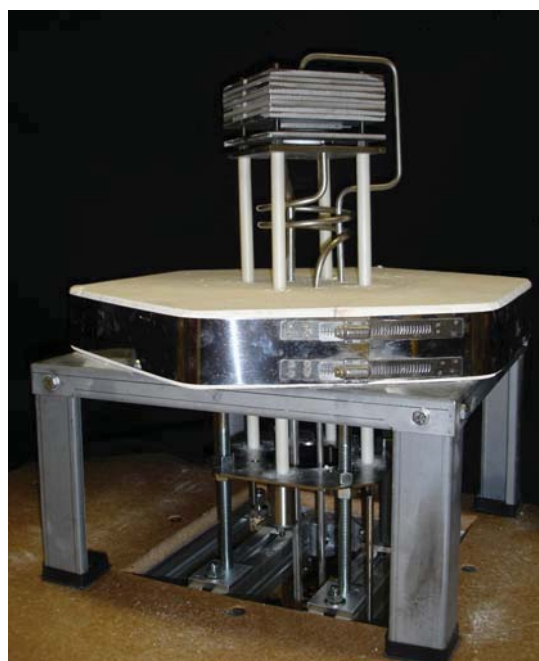


Figure 5. Test stand installed in furnace base.

## 2. Impedance Spectroscopy System

AC impedance spectroscopy data were obtained using a Solartron Modulab 2100A system. The system includes an integrated power supply, load, and data acquisition system that can be configured to control and analyze electrochemical experiments. The

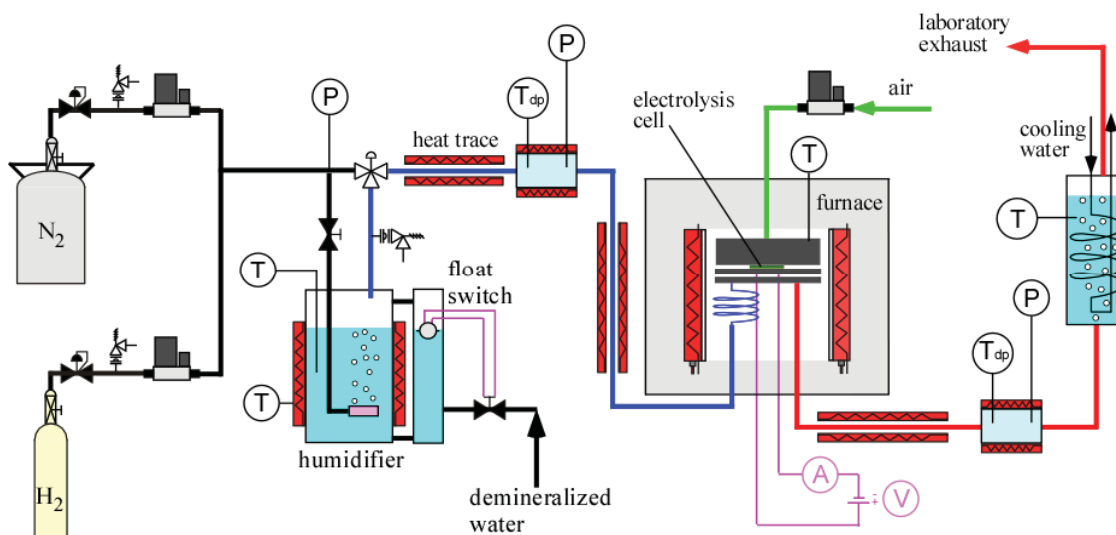


Figure 6. Process flow diagram for single-cell test apparatus.

Table 1. Hydrogen electrode reduction procedure.

step	Hold time (min)	H <sub>2</sub> Flow rate (sccm)	T <sub>dp</sub> (°C)	H <sub>2</sub> O flow rate (sccm)	N <sub>2</sub> flow rate (sccm)	Air flow rate (sccm)	T <sub>cell</sub> (°C)	y <sub>H2O</sub>
0 (heatup)	n/a	0	bypass	0	500	500	1°C/min	0
1	75	80	bypass	0	500	580	900	0
2	7.5	160	bypass	0	500	660	900	0
3	7.5	160	22	20.8	500	660	900	0.031
4	5	320	22	25.9	500	820	900	0.031
5	5	500	22	23.7	250	750	900	0.031
6	5	500	22	15.8	0	500	900	0.031

basic system contains a potentiostat that is capable of driving and controlling a cell or stack in the voltage and current ranges of -8 to +8 V and -0.3 to +0.3 A respectively. Up to 7 additional instrumentation modules may be added to the system to perform other operations such as frequency response analysis and electrical impedance spectroscopy, or to extend the range over which measurements may be taken via a power booster module. Control of the Modulab system is performed via the native Modulab software which allows for full automation of experiments. Several types of measurements may be performed sequentially within a single experiment.

Impedance spectra were obtained with the single in the fuel cell mode, the electrolysis mode, and at open cell conditions via an integrated frequency response analyzer. A Solartron Booster 12V/20A was used to ensure sufficient power/load were available to the cell during fuel cell mode for power dissipation while sinking sufficient current during electrolysis operations. An applied potential was maintained for each mode of operation such that for fuel cell mode, a potential less than the open cell voltage was maintained across the cell, and for electrolysis, a potential greater than the open cell voltage was maintained. The fuel cell and electrolysis cell potentials used for the spectra were 0.7144 V and 1.0884 V respectively, which corresponded to a cell current of  $\pm 6$  A. EIS spectra were obtained using a superimposed sweeping 50 mV modulated signal over a frequency range of 100 kHz down to 30 mHz.

### 3. Cell Reduction Procedure

The electrode-supported cells tested in this study are supported by the porous 1.5 mm thick steam/hydrogen electrode whose initial composition is nickel oxide and YSZ. The nickel oxide must be reduced to nickel metal in order for the electrode to become electronically conductive. This reduction process is accomplished by exposing the electrode to increasing levels of hydrogen gas at 900°C, as indicated in Table 1. The initial heatup of the cell (step 0) is performed under inert gas at a heatup rate of 1°C/min to 900°C. The cell is then exposed to varying nitrogen/hydrogen/steam gas mixtures for the time durations indicated in the table. The steam was introduced by bubbling the nitrogen/hydrogen gas mixture through a room-temperature water bath (humidifier). The corresponding steam flow rates can be calculated based on the nitrogen and hydrogen flow rates and the bath temperature. These calculated steam flow rate values are listed in the table. The steam/hydrogen electrode of the reduced cell is silver/gray in color.

### 4. Test Procedure

After the cell reduction procedure is completed, performance testing can be initiated. Test conditions can be determined as follows. Specify the cell active area and maximum

desired current density. The nominal active area for the cells in this study is 16 cm<sup>2</sup>. The maximum current density is usually set such that the maximum cell voltage is near the thermal neutral voltage ( $V_{tn} = 1.287$  V at 800°C). Once the current density and cell area are known, the total cell current is known ( $I = i \times A_{cell}$ ) and the molar hydrogen production rate can be determined directly from Faraday's law:

$$Q_{M,H_2,prod} = \frac{I}{2F} \quad (1)$$

This molar value can be converted to a standard volumetric flow rate (e.g., sccm) by dividing by the standard-state molar density,  $\rho_M = 44.615$  mol/m<sup>3</sup>.

A desired value for maximum steam utilization can then be specified. Depending on the objective of the test, this value could range from 0.2 – 0.9. Low values of steam utilization generally yield better cell performance in the electrolysis mode. High values can cause localized steam starvation and corresponding reduced cell performance. Analysis of large-scale systems has indicated that overall system performance drops off for steam utilization values below ~0.5, but is fairly flat above that value (22). Once the desired steam utilization is specified, the required inlet steam flow rate can be determined from

$$Q_{H_2O,i} = \frac{Q_{H_2,prod}}{U_{H_2O}} \quad (2)$$

Since steam is introduced in this case using a humidifier, the steam flow rate depends on both the inlet dewpoint temperature, which is approximately the same as the humidifier bath temperature, and the flow rates of nitrogen and hydrogen. So the inlet dewpoint temperature must be specified. Nitrogen is included as an inert carrier gas to enable higher total steam flow rates and to allow for independent variation of the steam and hydrogen compositions in the inlet flow.

For testing in the electrolysis mode, a reasonably high inlet dewpoint temperature is required, typically 60 – 70°C. Once the inlet dewpoint temperature is specified, the corresponding inlet mole fraction of steam is given by

$$y_{H_2O,i} = \frac{P_{sat}(T_{dpi})}{P_T} \quad (3)$$

where  $P_{sat}(T_{dpi})$  is the vapor pressure of steam at the specified inlet dewpoint temperature, obtained from an appropriate correlation such as the Antoine equation. The total required inlet gas flow of nitrogen plus hydrogen can then be obtained from

$$Q_{gas,i} = Q_{H_2O,i} \frac{1 - y_{H_2O,i}}{y_{H_2O,i}} \quad (4)$$

The inlet flow rate of hydrogen can be determined by specifying the desired inlet mole fraction of hydrogen, typically 0.1 – 0.2. Inlet hydrogen is required to maintain reducing conditions on the nickel cermet material. The respective flow rates of hydrogen and nitrogen are then obtained from:

$$Q_{H_2,i} = \frac{y_{H_2,i}}{y_{H_2O,i}} Q_{H_2O,i} \quad (5)$$

$$Q_{N_2} = Q_{gas,i} - Q_{H_2,i} \quad (6)$$



Air is typically used on the oxygen side of the cell as a sweep gas in order to prevent buildup of pure oxygen. The flow rate of air is scaled with respect to the oxygen production rate,

$$Q_{O_2,prod} = Q_{H_2,prod} / 2 \quad (7)$$

as follows:

$$Q_{air} = \frac{N_{O_2prod} Q_{O_2,prod}}{y_{O_2,air}} \quad (8)$$

where  $N_{O_2prod}$  is a factor indicating the number of oxygen production equivalents desired in the sweep air and  $y_{O_2,air}$  is the mole fraction of oxygen in the sweep gas ( $y_{O_2,air} = 0.21$ ). We typically use  $N_{O_2prod} = 1$ , which yields an outlet sweep gas mole fraction of oxygen equal to 0.347. Once the cell operating temperature is selected, the test conditions are fully specified.

## 5. Preliminary Results

Initial cell characterization was measured through a series of DC potential sweeps obtained over a range of inlet dewpoint values from 20 - 75°C. The sweeps were obtained with a hydrogen inlet gas flow rate of 500 sccm, a nitrogen inlet gas flow rate of 500 sccm, and an inlet air flow rate of 1000 sccm on the oxygen side of the cell. Voltage-current density results are presented in Fig. 7. These curves indicate the effect of steam content on the open-cell potential, which is below 0.9 V for  $T_{dpi} = 75^\circ\text{C}$  and above 1.0 V for  $T_{dpi} = 20^\circ\text{C}$ . The sweeps obtained with the highest steam content are nearly linear over the entire voltage range, from fuel cell mode through electrolysis mode. The  $T_{dpi} = 50^\circ\text{C}$  sweep exhibits evidence of steam starvation at relatively low current density in the electrolysis mode. The  $T_{dpi} = 20^\circ\text{C}$  sweep was obtained only in the fuel cell mode since there is insufficient steam content to support electrolysis in this case. This sweep shows significant curvature at low current density in the fuel cell mode, possibly associated with activation overpotential.

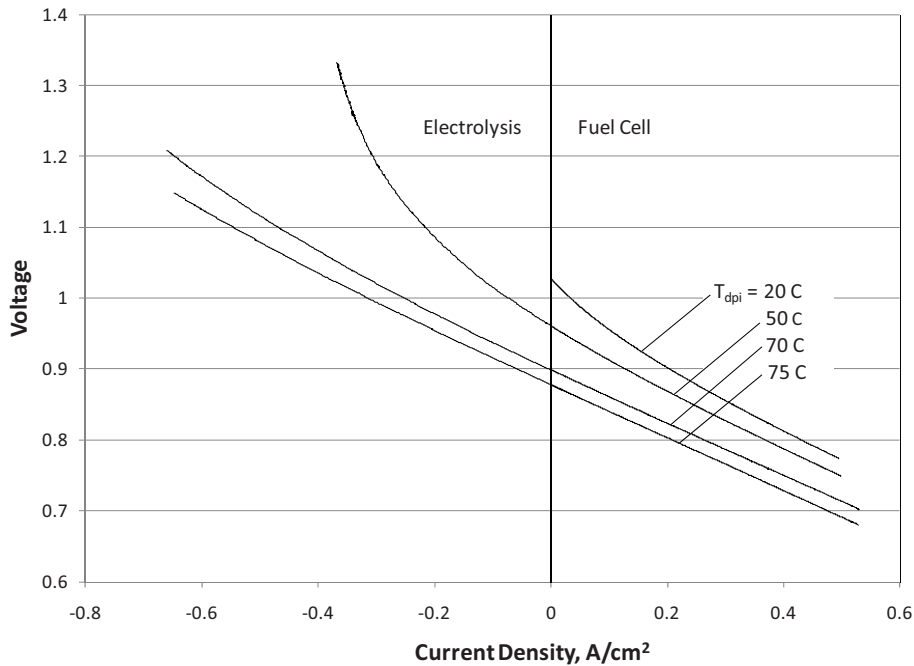


Figure 7. Initial polarization curves, dependence on steam content.

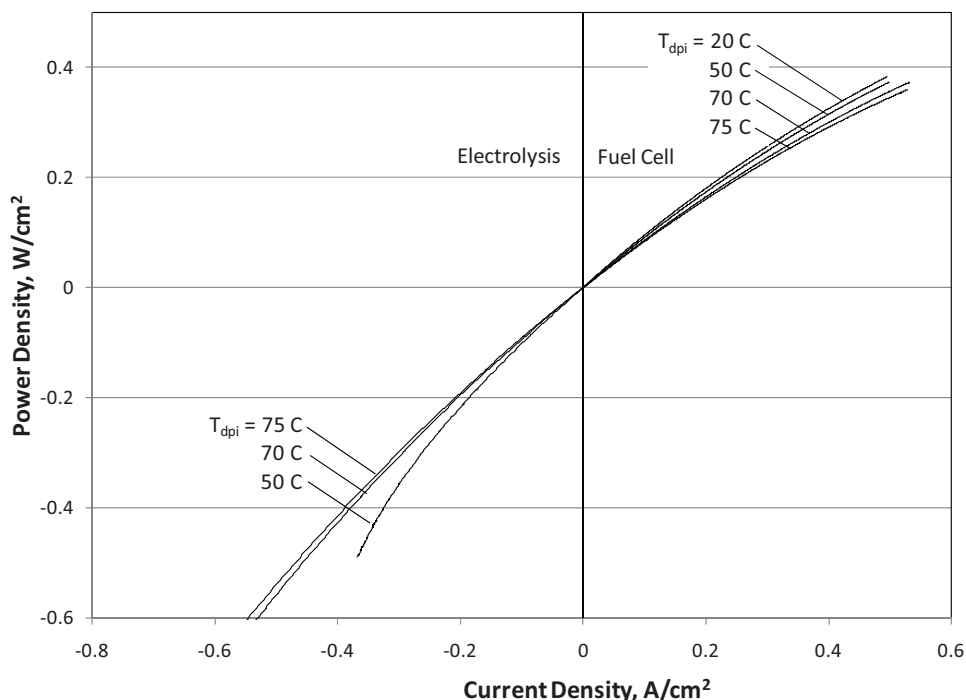


Figure 8. Power densities, dependence on steam content.

Power densities in the fuel cell and electrolysis modes, corresponding to the Vi curves of Fig. 7 are presented in Fig. 8. Power density magnitudes in the both modes are highest for low steam content and lowest for high steam content. From this perspective low steam content is preferable in the fuel cell mode and high steam content is preferable in electrolysis mode. The higher power densities in the fuel cell mode at low steam content is due to the higher open-cell potential associated with low steam.

Area-specific resistances in both modes of operation are lowest with high steam content, as shown in Fig. 9. These curves also correspond to the Vi curves of fig. 7. ASR values in the fuel cell mode for sweeps with high steam content are quite low, around 0.35  $\text{Ohm}\cdot\text{cm}^2$ . With high steam content, ASR values are nearly flat from the fuel cell mode to the electrolysis mode, but in all cases ASR values climb at the highest current density magnitudes in the electrolysis mode. ASR values are flat or decreasing at the highest current densities in the fuel cell mode. This apparent improvement of fuel-cell-mode performance, at least in terms of ASR, with high steam content has been observed by others (23).

Impedance spectra were obtained in the fuel cell mode, the electrolysis mode, and at open-cell conditions over a frequency range of 100 kHz – 30 mHz. The fuel cell and electrolysis spectra were obtained with the same magnitude of current density, 0.35  $\text{A}/\text{cm}^2$ . Gas flow rates were the same as those used for the initial sweeps, and the inlet dewpoint temperature was 70°C, which provides a steam mole fraction very close to 50%. The spectra were obtained after about 200 hours of test time, so some performance degradation had already occurred. Results are presented in Fig. 10 in terms of a Nyquist plot. The spectra exhibit a very well defined high frequency arc as well as a large low frequency arc. Low-frequency intercepts correspond nicely to the respective overall ASR values corresponding to this test time, ~0.45 in the fuel cell mode and ~0.55 in the electrolysis mode. Spectra for the fuel cell mode and open-cell mode are similar, with the exception of the highest frequencies. The spectra all indicate significant low-frequency contributions associated with gas conversion. Overall polarization resistances based on these spectra are about 0.44  $\text{Ohm}\cdot\text{cm}^2$  in the electrolysis mode and 0.30  $\text{Ohm}\cdot\text{cm}^2$  in the fuel cell mode.

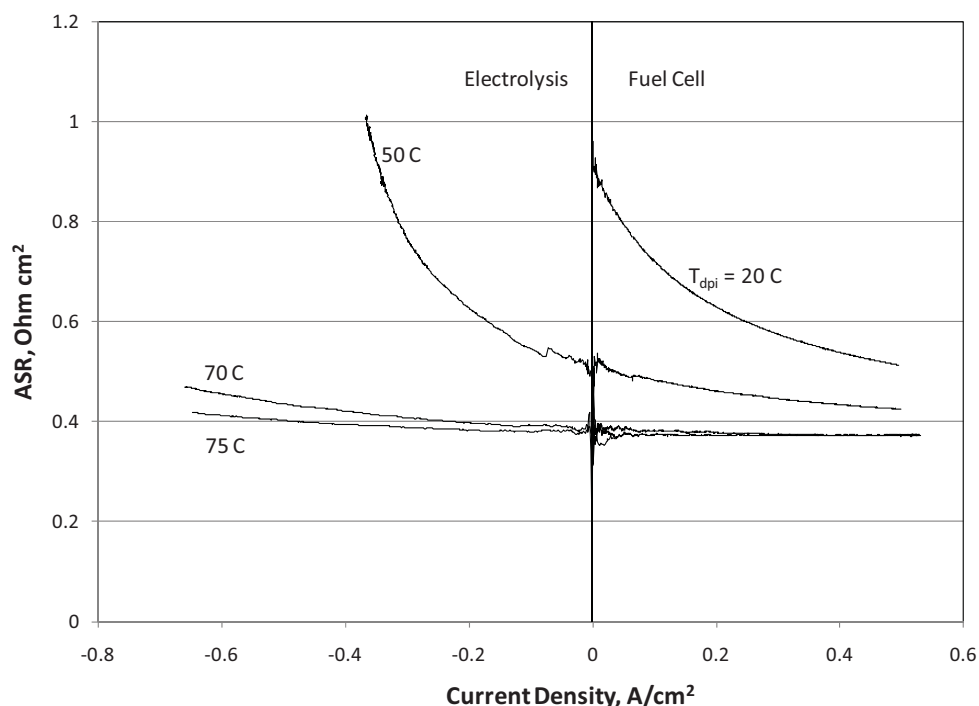


Figure 9. Area-specific resistances as a function of current density, effect of steam content.

Long-duration cell performance was measured over more than 500 hours. Gas flow rates for the long-duration tests was the same as for the initial sweeps. The first 170 hours were run in the fuel cell mode, followed by operation in the electrolysis mode. The fuel cell portion was operated in the constant current mode at 6.0 A, or  $0.35 \text{ A/cm}^2$ . The electrolysis long-duration test was performed in the constant-voltage mode, with an initial current density of  $0.35 \text{ A/cm}^2$ . Results of the long-duration testing are presented in Fig. 11. The first 125 hours of operation in the fuel cell mode exhibited essentially no degradation. At the 125-hour mark, an excursion in ASR occurred, due to an unknown event. After about 170 hours, cell operation was switched to the electrolysis mode. After this mode switch, degradation occurred at a nearly constant rate, with the cell ASR value increasing from  $0.51$  to  $0.87 \text{ Ohm cm}^2$  over about 300 hours. This rapid degradation will be investigated further with additional testing.

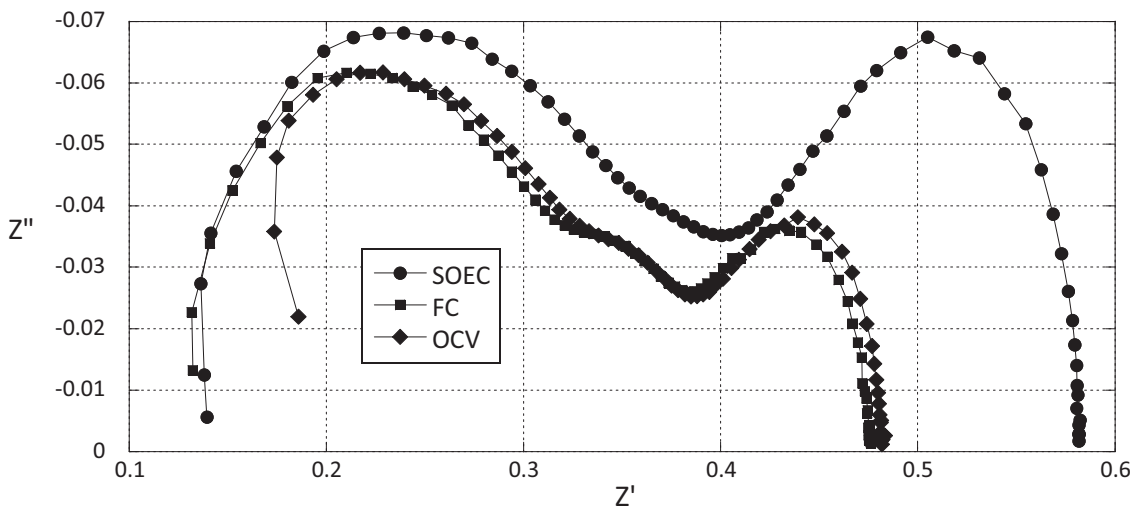


Figure 10. Impedance spectra, fuel cell mode, electrolysis mode, and open-cell.

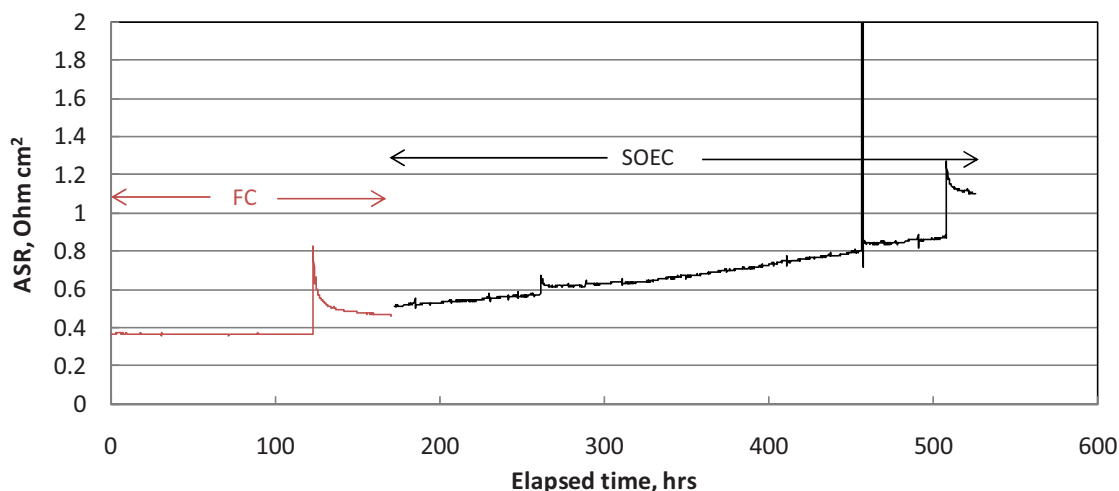


Figure 11. Long-term degradation results, fuel-cell and electrolysis modes.

## 6. Summary and Conclusions

Initial performance characterization of nickel cermet-supported cells operating in both the fuel cell and electrolysis modes has been completed. Results indicate excellent initial performance in both modes of operation, with an initial ASR value of  $\sim 0.35 \text{ Ohm cm}^2$  in both modes for the case of high steam content. ASR values were shown to increase with reduced steam content in both modes of operation. Power densities are most favorable for low steam content in the fuel cell mode and high steam content in the electrolysis mode. Impedance spectra exhibit well defined low-frequency and high-frequency arcs for these cell. Long duration tests indicate significantly higher degradation rates in the electrolysis mode compared to the fuel cell mode.

## Acknowledgements

This work was supported by the U.S. Department of Energy, Office of Nuclear Energy, Nuclear Hydrogen Initiative and Next Generation Nuclear Plant Programs under DOE Operations Office Contract DE-AC07-05ID14517.

## References

- (1) Forsberg, C. W., "The Hydrogen Economy is Coming. The Question is Where?" *Chemical Eng. Progress*, Dec. 2005, pp. 20-22.
- (2) Lewis, D., "Hydrogen and its relationship with nuclear energy," *Progress in Nuclear Energy*, Vol. 50, pp. 394-401, 2008.
- (3) Kruger, P., "Nuclear Production of Hydrogen as an Appropriate Technology," *Nuclear Technology*, Vol. 166, pp. 11-17, 2009.
- (4) Forsberg, C. W., "Future hydrogen markets for large-scale hydrogen production systems," *Int. J. Hydrogen Energy*, Vol. 32, pp. 431-439, 2007.
- (5) Duffey, R. B., "Nuclear production of hydrogen: When worlds collide," *International Journal of Energy Research*, Vol. 33, pp. 126-134, 2009.
- (6) Granovskii, M., Dincer, I., and Rosen, M. A., "Greenhouse gas emissions reduction by use of wind and solar energies for hydrogen and electricity production: economic factors," *Int. J. Hydrogen Energy*, V. 32, 2007, pp. 927-931.

- (7) Rand, D. A. J., and Dell, R. M., *Hydrogen Energy: Challenges and Prospects*, Royal Society of Chemistry, 2008.
- (8) Floch, P-H., Gabriel, S., Mansilla, C., and Werkoff, F., "On the production of hydrogen via alkaline electrolysis during off-peak periods," *Int. J. Hydrogen Energy*, Vol. 32, 2007, pp. 4641-4647.
- (9) Schultz, K. R., Brown, L. C., Besenbruch, G. E. and Hamilton, C. J., "Large-Scale Production of Hydrogen by Nuclear Energy for the Hydrogen Economy," Report GA-A24265, Feb. 2003, 22p.
- (10) O'Brien, J. E., Stoots, C. M., Herring, J. S., and Hartvigsen, J. J., "Performance of Planar High-Temperature Electrolysis Stacks for Hydrogen Production from Nuclear Energy," *Nuclear Technology*, Vol. 158, pp. 118 - 131, May, 2007.
- (11) Steinfeld, A. "Solar thermochemical production of hydrogen," *Solar Energy*, V 78, No 5, pp. 603-615, May 2005.
- (12) Southworth, F., Macdonald, P. E., Harrell, D. J., Park, C. V., Shaber, E. L., Holbrook, M. R., and Petti, D. A., "The Next Generation Nuclear Plant (NGNP) Project," Proceedings, Global 2003, pp. 276-287, 2003.
- (13) Schultz, K., Sink, Pickard, P., Herring, J. S., O'Brien, J. E., Buckingham, R., Summers, W., and Michele Lewis, M., "Status of the US Nuclear Hydrogen Initiative," Proceedings of ICAPP 2007, Paper 7530, Nice, France, May 13-18, 2007; *The Nuclear Renaissance at Work*, V. 5, Societe Francaise d'Energie Nucleaire – ICAPP 2007, pp. 2932-2940.
- (14) Stoots, C. M., O'Brien, J. E., Condie, K., Moore-McAteer, L., Housley, G. K., Hartvigsen, J. J., and Herring, J. S., "The High-Temperature Electrolysis Integrated Laboratory Experiment," *Nuclear Technology*, April, 2009.
- (15) Varrin, R. D., Reifsneider, K., Scott, D. S., Irving, P., and Rolfson, G., "NGNP Hydrogen Technology Down-Selection; Results of the Independent Review Team Evaluation," Dominion Engineering report# R-6917-00-01, August, 2009.
- (16) Hauch, A. (2007). "Solid Oxide Electrolysis Cells – Performance and Durability," Ph.D. Thesis, Technical University of Denmark, Risø National Laboratory, Roskilde, Denmark.
- (17) Tanasini, P., Cannarozzo, M., Costamagna, P., Faes, A., Van Herle, J., Hessler-Wyser, A., Comninellis, C., "Experimental and theoretical investigation of degradation mechanisms by particle coarsening in sofc electrodes," *Fuel Cells*, v 9, n 5, p 740-752, October 2009.
- (18) Butz, B., Kruse, P., Stormer, H., Gerthsen, D., Muller, A., Wever, A., and Ivers-Tiffée, E., "Correlation between Microstructure and Degradation in Conductivity for Cubic Y2O3-doped ZrO2," *Solid State Ionics*, Vol. 177, Issue 37, pp. 3275-3284, 2006.
- (19) Marina, O. A., Pederson, L. R., Williams, M. C., Coffey, G. W., Meinhardt, K. D., Nguyen, C. D., and Thomsen, E. C., "Electrode Performance in Reversible Solid Oxide Fuel Cells, *J. Electrochemical Soc.*, Vol. 154, No. 5, pp. B452-B459, 2007.
- (20) Svensson, A. M., Sunde, S., and Nisancioglu, K., "Mathematical Modeling of Oxygen Exchange and Transport in Air-Perovskite-Yttria-Stabilized Zirconia Interface Regions," *J. Electrochemical Soc.*, Vol. 145, No. 4, pp. 1390-1400, April 1998.
- (21) Virkar, A. V., "Mechanism of Oxygen Electrode Delamination in Solid Oxide Electrolyzer Cells," *Int. J. Hydrogen Energy*, in review, 2010.
- (22) O'Brien, J. E., McKellar, M. G., and Herring, J. S., "Performance Predictions for Commercial-Scale High-Temperature Electrolysis Plants Coupled to Three Advanced Reactor Types," 2008 International Congress on Advances in Nuclear Power Plants, June 8-12, 2008, Anaheim, CA.
- (23) Kim P, Brett DJL, Brandon NP., "The effect of water content on the electrochemical impedance response and microstructure of Ni-CGO anodes for solid oxide fuel cells," *J Power Sources*, Vol. 189, pp. 1060-1065, 2009.